

Graph Neural Networks for Jamming Source Localization

Dania Herzalla(✉), Willian T. Lunardi, and Martin Andreoni

Technology Innovation Institute, Abu Dhabi, United Arab Emirates
 {dania.herzalla, willian.lunardi, martin.andreoni}@tii.ae

Abstract. Graph-based learning has emerged as a transformative approach for modeling complex relationships across diverse domains, yet its potential in wireless security remains largely unexplored. In this work, we introduce the first application of graph-based learning for jamming source localization, addressing the imminent threat of jamming attacks in wireless networks. Unlike geometric optimization techniques that struggle under environmental uncertainties and dense interference, we reformulate the localization as an inductive graph regression task. Our approach integrates structured node representations that encode local and global signal aggregation, ensuring spatial coherence and adaptive signal fusion. To enhance robustness, we incorporate an attention-based Graph Neural Network (GNN) that adaptively refines neighborhood influence and introduces a confidence-guided estimation mechanism that dynamically balances learned predictions with domain-informed priors. We evaluate our approach under complex Radio Frequency (RF) environments with varying sampling densities and signal propagation conditions, conducting comprehensive ablation studies on graph construction, feature selection, and pooling strategies. Results demonstrate that our novel graph-based learning framework significantly outperforms established localization baselines, particularly in challenging scenarios with sparse and obfuscated signal information. Our code is available at <https://github.com/daniaherzalla/gnn-jamming-source-localization>.

Keywords: Graph-based learning · Graph Neural Networks · Graph regression · Wireless security · Jamming source localization

1 Introduction

Graphs serve as a fundamental framework for representing complex relationships and interactions in real-world systems. Their versatility allows for the sophisticated modeling of diverse data types, driving their adoption across scientific and industrial domains such as molecular property prediction, social recommendation systems, and traffic forecasting. Many of the most successful machine learning applications, such as image, text, and speech processing, can be viewed as specialized cases of graph-based learning, underscoring the broad relevance and

transformative potential of graph representations in advancing machine learning methodologies [23]. Although graph-based learning has been explored in numerous domains, its application to wireless security remains relatively underexplored. In particular, jamming source localization, a task essential for mitigating the imminent threat posed by disruptive sources of interference to the availability of wireless communication, is yet to be explored through this application, presenting a novel avenue for research and application. In this study, we investigate the application of a novel graph-based learning framework to perform an inductive graph-level regression task to predict the location of a jamming source in complex RF operating environments.

The ubiquitous and growing dependence on wireless networks for applications ranging from everyday connectivity to mission-critical operations introduces significant security vulnerabilities. As jamming attacks transmit intentional interference signals across communication frequencies, they effectively lead to the degradation and severing of wireless links [15]. The repercussions of such attacks are severe, leading to failures in mission coordination, disruptions in essential services, and even operational hazards [28]. While countermeasures such as frequency hopping have been employed, their effectiveness is limited against advanced jammers such as reactive, follow-on, and barrage that adaptively pursue target frequencies and create dense interference across multiple channels [16]. Unlike avoidance techniques that passively adjust the network to evade interference, jamming source localization can provide a direct mitigation strategy. By accurately identifying the jammer’s position, network administrators can deploy targeted countermeasures such as physical neutralization, geofencing, or jamming suppression, restoring network reliability regardless of the changing dynamics of the jammer’s strategy [28].

Classical jamming localization methods rely on geometric and optimization-based techniques to estimate jammer positions. However, they degrade in real-world RF environments due to noise and multipath effects [13]. Their dependence on idealized propagation models limits adaptability to stochastic RF dynamics. To overcome these limitations, we introduce a novel graph-based formulation of the jamming localization problem, leveraging attention-based GNNs to adaptively extract spatial and signal-related patterns from measurements. Additionally, we propose Confidence-guided Adaptive Global Estimation (CAGE), a confidence-guided estimation mechanism that dynamically balances GNN-based predictions with domain-informed priors, improving robustness across varying deployment conditions. Rather than treating localization as a geometric optimization problem, we redefine it as a graph regression task, where node features encode key RF and spatial characteristics, and the graph structure captures local and global signal dependencies. Our contributions are as follows:

- We present the first application of GNNs to jamming source localization in wireless networks by reformulating the problem as a graph regression task.
- We propose a graph-based learning framework with structured node representations for local and global signal aggregation. We also introduce a

confidence-guided estimation mechanism to balance GNN predictions with domain-informed priors.

- We conduct comprehensive ablation studies on graph construction and model design, analyzing the impact of node connectivity, feature selection, pooling strategies, downsampling techniques, and graph augmentations on localization performance and model robustness.
- We benchmark against well-known localization methods in challenging environments, consistently outperforming established baselines, with emphasized improvements in scenarios characterized by sparse and obscured signal information.

The remainder of this paper is organized as follows. Section 2 reviews related work, highlighting existing approaches to jamming source localization and their limitations. Section 3 formally defines the problem, detailing the network configuration, jammer characteristics, and underlying assumptions. Section 4 presents a learning framework that dynamically integrates data-driven representations with inductive priors. Section 5 reports experimental results, demonstrating the effectiveness of our approach under various network conditions. Finally, we conclude by discussing key findings and future research directions.

2 Related Work

2.1 Jamming Source Localization

Jamming source localization has been widely studied under range-free and range-based algorithms. Range-free algorithms determine location information using network topology-related properties, without relying on the physical characteristics of incoming signals [10]. These methods are useful in infrastructure-limited environments, however, they suffer from degraded accuracy in sparse or unevenly distributed networks [28,25]. In contrast, range-based methods utilize geometric optimization to estimate the distance to the source using the measurement of various physical properties such as Received Signal Strength Indicator (RSSI), Time of Arrival (ToA), and Angle-of-Arrival (AoA) [10]. While these methods generally achieve higher accuracy, obtaining measurements such as ToA and AoA rely on specialized and calibrated hardware and are susceptible to errors where multipath effects introduce significant biases [29].

Many of the existing jammer localization approaches are validated under theoretical propagation models, such as free-space path loss, which fails to capture the complexities of real-world settings. Additionally, many evaluations do not encompass a diverse array of network attack scenarios, including irregular node placements, sparse samples, and long-range jamming attacks [14]. To address these limitations, we evaluate our method on diverse network configurations, leveraging the Log Distance Path Loss (LDPL) [6] model to account for realistic signal propagation conditions (see Appendix F).

As our method leverages spatial and signal information exclusively, we focus on methods that can similarly harness this information for localization. We

benchmark our approach against established range-free and range-based localization techniques: Weighted Centroid Localization (WCL) [25], Least Squares (LSQ) [28], Path Loss (PL) [12], Maximum Likelihood Estimation (MLE) [12], and Multilateration (MLAT) [30]. These baselines serve as reference points to assess the robustness and adaptability of our graph-based framework.

2.2 Graph Neural Networks for Localization

GNNs have demonstrated strong capabilities in regression tasks by capturing spatial dependencies within graph-structured data, such as in molecular property prediction and material science [11]. Beyond these domains, GNNs have also been applied to pose regression problems, including camera pose estimation [22] and human pose tracking [31], where they refine node and edge representations to improve motion prediction and spatial consistency. Their effectiveness in localization tasks has also gained attention, particularly in wireless and sensor network applications. GNNs have been applied to RF-based localization, including WiFi fingerprinting-based indoor localization [8], where GNNs leverage RSSI signals to construct graphs and improve positioning accuracy. More recent works extend GNNs for network localization beyond Wi-Fi, addressing challenges such as dynamic network topologies and mobility-induced signal variation [6].

While these advancements highlight the growing potential of GNNs for network localization, their application to jamming source localization remains unexplored. This gap presents an opportunity to adapt GNNs to interference localization, addressing unique challenges in adversarial conditions.

3 Problem Definition

The problem addressed in this study is the localization of a wireless jammer, an adversarial interference source that disrupts communications by emitting high-power signals to degrade legitimate wireless communication.

Network Configuration The network consists of N devices, either static or dynamic, deployed in a D -dimensional space, where $\mathcal{A} \subset \mathbb{R}^D$ defines the geographic area of interest and $N \geq 1$. Each device i records signal measurements over time, forming a set of samples:

$$\mathcal{S}_i = \{s_i^1, s_i^2, \dots, s_i^T\}, \quad s_i^t = (\mathbf{x}_i^t, \eta_i^t)$$

where s_i^t denotes a measurement taken at position \mathbf{x}_i^t with an associated noise floor value η_i^t in dBm at time t . Note that η_i^t , referred to as the *noise floor*, is commonly treated as jamming signal strength, where here it represents the combined effect of jammer interference and baseline environmental noise floor. Signal attenuation and propagation effects are modeled using the empirical LDPL model to simulate Non-line-of-sight (NLOS) conditions; refer to Appendix F for details.

This formulation accommodates both *static* and *dynamic* sampling scenarios. In the static case, devices remain at fixed locations but are likely distributed over

space. In contrast, in the dynamic case, devices move through space, collecting measurements at different positions over time.

Jammer Characteristics The jammer is located at an unknown position $\mathbf{x}_j \in \mathcal{A}$ and emits interference signals that elevate the noise floor of nearby devices. The interference strength varies spatially due to distance attenuation and propagation effects such as shadowing, reflections, and multipath fading. The sampled region, denoted as $\mathcal{R} \subseteq \mathcal{A}$, is the subset of \mathcal{A} where devices collect noise floor measurements. Although the jammer's position satisfies $\mathbf{x}_j \in \mathcal{A}$, it does not necessarily hold that $\mathbf{x}_j \in \mathcal{R}$, i.e., $\mathbf{x}_j \in \mathcal{A} \setminus \mathcal{R}$ is possible. We evaluate localization methods in scenarios where the jammer affects areas beyond the sampled region, testing their ability to infer positions outside direct measurement zones.

Objective Given the set of samples collected by N devices, denoted as $\mathcal{S} = \{\mathcal{S}_1, \mathcal{S}_2, \dots, \mathcal{S}_N\}$, the goal is to infer \mathbf{x}_j based on the spatial distribution of measured noise floor levels. This problem is inherently challenging due to incomplete and noisy measurements, environmental uncertainty affecting signal propagation, complex spatial correlations between noise floor levels and jammer interference, and the need to generalize beyond observed regions where no direct measurements are available.

4 Graph-Structured Learning for Jammer Localization

We structure the above problem as a graph representation to systematically model spatial relationships and signal attenuation. Given the set of collected measurements $\mathcal{S} = \{\mathcal{S}_1, \mathcal{S}_2, \dots, \mathcal{S}_N\}$, we represent the sampled signal space as a graph $G = (V, E)$, where nodes in V correspond to individual measurement instances $s_i^t \in \mathcal{S}_i$, and edges E define spatial relationships between them. Edges are established using K-Nearest Neighbors (KNN), where for each node v_i , an edge set is constructed as $E = \{(v_i, v_j) \mid v_j \in \mathcal{N}_k(v_i)\}$, where $\mathcal{N}_k(v_i)$ denotes the set of k nearest neighbors of v_i in the Euclidean space. To enforce the spatial attenuation principle of jamming signals, each edge (v_i, v_j) is assigned a weight w_{ij} that decays exponentially with the Euclidean distance as:

$$w_{ij} = \frac{e^{-d_{ij}} (e - e^{d_{ij}})}{e - 1}, \quad (1)$$

where $d_{ij} = \frac{\|\mathbf{x}_i - \mathbf{x}_j\|}{d_{\max}}$ is the normalized Euclidean distance between nodes v_i and v_j , with $d_{\max} = \max_{(v_i, v_j) \in E} \|\mathbf{x}_i - \mathbf{x}_j\|$.

Since message passing in the graph relies on node and edge attributes, we define a structured representation that incorporates both spatial and signal characteristics. Each node $i \in V$ is assigned a feature vector:

$$X_i = (\tilde{\eta}_i, \mathbf{x}_i^{\text{sph}}, \mathbf{x}_i^{\text{cart}}, \mathcal{F}_i^{\text{local}}). \quad (2)$$

where $\tilde{\eta}_i$ is the normalized noise floor value and $\mathbf{x}_i^{\text{sph}}$ represents the normalized angular representation:

$$\mathbf{x}_i^{\text{sph}} = (r_i, \sin \theta_i, \cos \theta_i, \sin \phi_i, \cos \phi_i), \quad (3)$$

where r_i is the radial distance from the origin, and (θ_i, ϕ_i) are the azimuth and elevation angles of the measured position. We additionally incorporate the normalized cartesian coordinate representation $\mathbf{x}_i^{\text{cart}} = (\tilde{x}_i, \tilde{y}_i, \tilde{z}_i)$ to maintain direct Euclidean relationships between nodes.

To encode spatial correlations and local noise floor variations within the graph, we define $\mathcal{F}_i^{\text{local}}$, which characterizes the local noise floor distribution within each node's neighborhood:

$$\mathcal{F}_i^{\text{local}} = \{\text{median}(\eta_{\mathcal{N}_k(i)}), \max(\eta_{\mathcal{N}_k(i)}), \Delta\eta_i, \mathbf{x}_i^{\text{wcent}}, d_i^{\text{wcent}}\},$$

where $\text{median}(\eta_{\mathcal{N}_k(i)})$ and $\max(\eta_{\mathcal{N}_k(i)})$ provide local statistical summaries of the noise floor levels, $\Delta\eta_i$ represents the deviation of the node's noise level from the mean noise level within its neighborhood, and $\mathbf{x}_i^{\text{wcent}}$ and d_i^{wcent} correspond to the *local weighted centroid* and its distance from the node v_i , respectively:

$$\mathbf{x}_i^{\text{wcent}} = \frac{\sum_{j \in \mathcal{N}_k(i)} \eta'_j \mathbf{x}_j}{\sum_{j \in \mathcal{N}_k(i)} \eta'_j}, \quad d_i^{\text{wcent}} = \|\mathbf{x}_i - \mathbf{x}_i^{\text{wcent}}\|, \quad \Delta\eta_i = \eta_i - \frac{1}{|\mathcal{N}_k(i)|} \sum_{j \in \mathcal{N}_k(i)} \eta_j,$$

where $\eta'_j = 10^{\eta_j/10}$ represents the noise floor level converted to linear scale.

For dynamic scenarios where devices move while collecting measurements, the graph representation is extended to incorporate temporal dependencies. Each node $i \in V$ retains its spatial attributes while additionally capturing motion through two features: the *direction vector* and the *temporal signal variation*. These measurements, computed between consecutive positions, are given, respectively, as:

$$\mathbf{d}_i = \mathbf{x}_i^{t+1} - \mathbf{x}_i^t, \quad \Delta\eta_i^{\text{temp}} = \eta_i^{t+1} - \eta_i^t.$$

The final node feature vector for dynamic scenarios is given by:

$$X_i = (\tilde{\eta}_i, \mathbf{x}_i^{\text{sph}}, \mathbf{x}_i^{\text{cart}}, \mathcal{F}_i^{\text{local}}, \mathbf{d}_i, \Delta\eta_i^{\text{temp}}). \quad (4)$$

4.1 Learning Spatial Relations with Attention-Based Graphs

Graph-based learning enables the model to capture structured dependencies in the jammer interference field, allowing for improved generalization across spatial regions. However, effective learning in this setting requires handling two key challenges: (1) signal measurements are inherently noisy due to environmental conditions, leading to unreliable observations, and (2) the importance of neighboring nodes varies depending on both their spatial proximity and their reliability in capturing interference effects. Traditional GNN architectures, such as Graph Convolutional Networks (GCNs) [7], rely on uniform neighborhood aggregation and struggle to capture the varying reliability of spatially adjacent

nodes. Our approach follows Graph Attention Network (GAT) [24], incorporating an adaptive weighting mechanism that dynamically refines neighborhood influence, ensuring that message passing prioritizes nodes carrying more reliable signal information while attenuating contributions from potentially misleading observations.

Let $X \in \mathbb{R}^{|V| \times F}$ represent the matrix of raw node features, where each node v_i has an initial feature vector $h_i^{(0)} = X_i \in \mathbb{R}^F$. Before computing attention, node features are first transformed at each layer l using a learnable weight matrix $\mathbf{W}^{(l)}$. The updated node representation at layer $l + 1$ is computed through the aggregation function denoted as:

$$h_i^{(l+1)} = \text{ReLU} \left(\sum_{j \in \mathcal{N}_i} \alpha_{ij}^{(l)} \mathbf{W}^{(l)} h_j^{(l)} \right). \quad (5)$$

The attention coefficients $\alpha_{ij}^{(l)}$, weighted by w_{ij} , determine the relative importance of each neighboring node v_j to node v_i and are computed as:

$$\alpha_{ij}^{(l)} = \frac{w_{ij} \exp \left(\text{LeakyReLU} \left(\mathbf{a}^T [\mathbf{W}^{(l)} h_i^{(l)} \parallel \mathbf{W}^{(l)} h_j^{(l)}] \right) \right)}{\sum_{k \in \mathcal{N}(i)} w_{ik} \exp \left(\text{LeakyReLU} \left(\mathbf{a}^T [\mathbf{W}^{(l)} h_i^{(l)} \parallel \mathbf{W}^{(l)} h_k^{(l)}] \right) \right)}, \quad (6)$$

where $\mathbf{a} \in \mathbb{R}^{2F'}$ is a learnable attention weight vector, with $2F'$ corresponding to the concatenation of intermediate node embeddings of dimension F' . Here, $(\cdot)^T$ denotes transposition, \parallel represents vector concatenation, and w_{ij} is given by Equation (1). In our implementation, we utilize multi-head attention as originally proposed in [24], where multiple independent attention mechanisms operate in parallel. The resulting node embeddings are concatenated across attention heads, except in the final layer, where they are averaged.

4.2 Supernode-Guided Adaptive Estimation

Prior work [25] establishes that WCL, a simple localization method based on weighted averaging of anchor positions, achieves low localization error when node density around jammer's position is high and placement is radially symmetric, with error decreasing as the number of nodes increases. Building on this, we expand the graph definition to incorporate WCL as a domain-informed prior, leveraging it under dense and symmetrical sampling conditions while introducing an adaptive confidence weighting mechanism for effective integration within the learning framework.

Global Context Encoding with Domain-Guided Priors We extend the graph representation $G = (V, E)$ by introducing a *supernode* v_s , which encodes a structured global prior by representing the weighted centroid of the measurement space based on noise floor levels. The augmented graph is defined as:

$$G' = (V', E'), \quad \text{where} \quad V' = V \cup \{v_s\}, \quad E' = E \cup \{(v_i \rightarrow v_s) \mid v_i \in V\}. \quad (7)$$

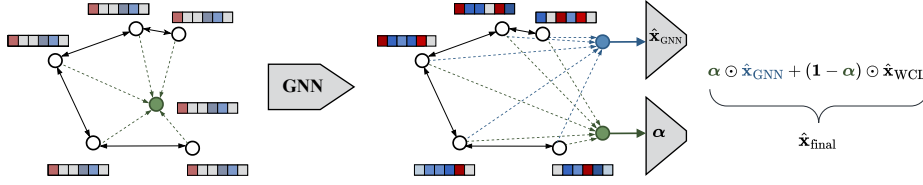


Fig. 1: Overview of the proposed jammer localization framework. A graph is constructed from noise floor measurements, where nodes represent signal instances, and edges capture spatial relationships. The encoder processes the graph to learn spatial correlations. The final jammer position is estimated through an adaptive combination of the GNN-based prediction and a WCL prior, controlled by a learned confidence weight α .

Each node $v_i \in V$ is connected to the supernode via a directed edge ($v_i \rightarrow v_s$) with weight w_{is} given by Equation (1). This connectivity structure ensures that the supernode functions as a global aggregator, primarily influencing the computation of a confidence weight α (later defined in Equation (12)) while remaining decoupled from the GNN regression process, thereby preventing direct bias from the WCL prior. The spatial position and noise level of the supernode are defined as:

$$\mathbf{x}_{\text{super}} = \frac{\sum_{i \in V} w_i \mathbf{x}_i}{\sum_{i \in V} w_i}, \quad \eta_{\text{super}} = \frac{\sum_{i \in V} w_i \eta_i}{\sum_{i \in V} w_i}, \quad \text{where } w_i = \frac{\eta'_i}{\sum_{j \in V} \eta'_j}. \quad (8)$$

Here, w_i represents the normalized weight assigned to each node v_i . Since the feature vector for each node, as defined in Equation 2, is a function of position, noise, and neighboring nodes, we also expand the feature representation for v_s .

Confidence-Guided Adaptive Position Estimation The estimated jammer position is computed as a five-tuple normalized angular representation combining the GNN-based prediction with the domain-informed WCL prior. The GNN-based position estimate is obtained by applying a linear transformation to a pooled representation of the node embeddings:

$$\hat{\mathbf{x}}_{\text{GNN}} = \mathbf{W}_{\text{GNN}} h_{\text{graph}} + \mathbf{b}_{\text{GNN}}, \quad (9)$$

where $\hat{\mathbf{x}}_{\text{GNN}} = (\hat{r}, \hat{s}_\theta, \hat{c}_\theta, \hat{s}_\phi, \hat{c}_\phi)$ represents the predicted position, with $\mathbf{W}_{\text{GNN}} \in \mathbb{R}^{5 \times F'}$ and $\mathbf{b}_{\text{GNN}} \in \mathbb{R}^5$ as learnable parameters. The graph representation h_{graph} of G' is computed using an element-wise max pooling operation over all node embeddings, excluding the supernode:

$$h_{\text{graph}} = \max_{v_i \in V} h_i^{(L)}, \quad (10)$$

where $h_i^{(L)}$ is the final embedding of node v_i after L layers of attention-based aggregation given in Equation (5). To determine the confidence weights $\alpha =$

$(\alpha_1, \alpha_2, \alpha_3, \alpha_4, \alpha_5)$, the supernode representation h_{super} is passed through a linear transformation followed by a sigmoid activation:

$$\boldsymbol{\alpha} = \sigma(\mathbf{W}_\alpha h_{\text{super}} + \mathbf{b}_\alpha), \quad (11)$$

where $\boldsymbol{\alpha} \in \mathbb{R}^5$ is a five-dimensional confidence vector, with each α_d corresponding to one of the five output components in the normalized angular representation. The parameters $\mathbf{W}_\alpha \in \mathbb{R}^{5 \times F'}$ and $\mathbf{b}_\alpha \in \mathbb{R}^5$ are learnable, and sigmoid $\sigma(\cdot)$ ensures that $0 < \alpha_d < 1$. Finally, the final predicted jammer position is computed as:

$$\hat{\mathbf{x}}_{\text{final}} = \boldsymbol{\alpha} \odot \hat{\mathbf{x}}_{\text{GNN}} + (\mathbf{1} - \boldsymbol{\alpha}) \odot \hat{\mathbf{x}}_{\text{WCL}}, \quad (12)$$

where \odot denotes element-wise multiplication, and $\hat{\mathbf{x}}_{\text{WCL}}$ is the five-tuple normalized angular representation of the WCL estimate.

This formulation allows the model to adaptively balance the reliance on the GNN-based prediction and the structured WCL prior, ensuring robustness across varying sampling densities and spatial distributions. The corresponding graph-based formulation and adaptive position estimation process are illustrated in Figure 1, showing the transformation from raw signal measurements to the final position estimate through graph construction, GNN encoding, and confidence-weighted integration of the WCL prior.

4.3 Training Strategy and Loss Function

To enable adaptive estimation, we define a loss function that minimizes localization error by optimizing the weighted combination of the GNN-based estimate and the WCL prior. Given a batch of training instances \mathcal{B} , the loss function for adaptive estimation is formulated as:

$$\mathcal{L}_{\text{Adapt}} = \frac{1}{|\mathcal{B}|} \sum_{m \in \mathcal{B}} \left\| \hat{\mathbf{x}}_j^{(m)} - (\boldsymbol{\alpha}^{(m)} \odot \hat{\mathbf{x}}_{\text{GNN}}^{(m)} + (\mathbf{1} - \boldsymbol{\alpha}^{(m)}) \odot \hat{\mathbf{x}}_{\text{WCL}}^{(m)}) \right\|^2, \quad (13)$$

where $\hat{\mathbf{x}}_j^{(m)}$ is the ground truth jammer position in the normalized angular representation, $\hat{\mathbf{x}}_{\text{GNN}}^{(m)}$ is the predicted position from the GNN model, and $\hat{\mathbf{x}}_{\text{WCL}}^{(m)}$ is the WCL-based position estimate. The confidence vector $\boldsymbol{\alpha}^{(m)} \in \mathbb{R}^5$ is learned from the supernode representation and dynamically balances the contribution of the two estimations.

Encouraging Independent Learning of the GNN Regressor While the confidence mechanism allows optimal weighting of WCL and GNN estimates, an inherent risk of optimizing Equation (13) alone is that the GNN regressor might learn primarily as a residual corrector for WCL rather than as an independent position estimator. To prevent this, we introduce an additional loss term that enforces direct learning of the jammer’s position by the GNN. This leads to the joint loss formulation:

$$\mathcal{L}_{\text{CAGE}} = \frac{1}{2} (\mathcal{L}_{\text{GNN}} + \mathcal{L}_{\text{Adapt}}) + \lambda \sum_{m \in \mathcal{B}} (1 - \alpha^{(m)})^2, \quad (14)$$

where

$$\mathcal{L}_{\text{GNN}} = \frac{1}{|\mathcal{B}|} \sum_{m \in \mathcal{B}} \left\| \hat{\mathbf{x}}_j^{(m)} - \hat{\mathbf{x}}_{\text{GNN}}^{(m)} \right\|^2. \quad (15)$$

Here, \mathcal{L}_{GNN} ensures that the GNN independently learns to predict the jammer’s position without being influenced by WCL, while $\mathcal{L}_{\text{Adapt}}$ (as defined in Equation (13)) optimizes the weighted combination of GNN and WCL estimates, ensuring that the model learns to assign appropriate confidence to each based on spatial conditions. The final term in Equation (14) penalizes deviations of $\alpha^{(m)}$ from 1, reducing over-reliance on WCL. For simplicity, we set $\lambda = 0$ in our experiments while retaining this term for flexibility.

Note that, in experimental evaluation, we refer to our proposed method as CAGE. For clarity in comparisons, Multilayer Perceptron (MLP), GCN, Principal Neighbourhood Aggregation (PNA) and GAT operate on graph G and are trained Equation (15) with the final estimate given by $\hat{\mathbf{x}}_{\text{GNN}}$, while CAGE is evaluated on the augmented graph G' and the adaptive confidence-weighted estimation, trained with Equation (14).

5 Experimental Evaluation

We evaluate CAGE across static and dynamic environments under the LDPL model. In the static setting (Section 5.1), fixed nodes with varying positions and densities are considered, with the jammer positioned either inside or outside the sampled region \mathcal{R} to study spatial effects. In the dynamic setting (Section 5.2), a device moves in 3D space, approaching and encircling the jammer to assess localization accuracy across angles and distances. Ablation studies in Section 5.3 and Appendix A evaluate the impact of node features, edge definitions, graph augmentations, global pooling mechanisms, and downsampling techniques. Further details on data generation, spatial arrangements, trajectory modeling, and signal propagation are provided in Appendix F, and additional analysis of confidence weighting is presented in Appendix B.

We compare CAGE against classical methods (WCL [28], LSQ [28], PL [12], MLAT [30], MLE [12], MLP) and graph learning-based methods (GCN [7], PNA [3], GAT [24]). As previously described, while MLP, GCN, PNA, and GAT operate on G , CAGE leverages augmented graph G' with the supernode, incorporating graph attention mechanisms alongside confidence-weighted estimation for adaptive localization. Models are trained using AdamW with a one-cycle cosine annealing scheduler. Hyperparameter tuning details, including model architectures and optimizer settings, are provided in Appendix E, while Appendix D describes the downsampling techniques applied in the dynamic experiments. All experiments are conducted over three independent trials with different random seeds to ensure robust evaluation, reporting the mean and standard deviation of Mean Absolute Error (MAE) and Root Mean Squared Error (RMSE) as the primary evaluation metrics.

Table 1: Jammer localization for static scenarios, reporting mean MAE and RMSE over three trials with different seeds. Results are split by different sampling strategies, where circle (C), triangle (T), rectangle (R), and random (RD) denote geometric distributions of sampling points relative to the jammer.

Method	Jammer within ($\mathbf{x}_j \in \mathcal{R}$)					Jammer outside ($\mathbf{x}_j \in \mathcal{A} \setminus \mathcal{R}$)					Mean	
	C	T	R	RD	Mean	C	T	R	RD	Mean		
MAE	WCL	37.7	40.2	27.2	35.7	35.2	138.6	169.0	170.1	164.2	160.5	97.9
	PL	122.2	83.3	90.6	82.0	94.5	289.4	247.3	290.6	267.4	273.7	184.1
	MLE	70.5	65.5	63.4	67.4	66.7	208.4	197.9	203.5	230.3	210.0	138.4
	MLAT	121.6	89.6	75.3	64.8	87.8	282.2	259.9	275.2	235.8	263.3	175.6
	LSQ	237.9	138.5	92.0	94.1	140.6	410.5	329.7	351.1	310.9	350.6	245.6
	MLP	37.1	31.3	24.7	29.5	30.7	60.1	78.2	78.5	84.1	75.2	53.0
	GCN	35.5	30.7	25.9	35.3	31.9	57.5	75.5	77.4	85.4	74.0	53.0
	PNA	34.3	27.7	21.9	26.7	27.7	56.5	72.7	74.1	79.4	70.7	49.2
	GAT	33.3	27.4	21.5	27.2	27.4	55.8	72.0	73.5	77.9	69.8	48.6
	CAGE	28.4	23.6	19.8	25.0	24.2	46.5	61.6	65.1	68.8	60.5	42.5
RMSE	WCL	53.6	65.6	39.7	54.1	53.3	201.6	241.1	254.6	234.0	232.8	143.1
	PL	159.5	115.0	121.3	114.6	127.6	357.3	314.4	365.2	336.2	343.3	235.5
	MLE	123.2	112.5	116.5	362.3	178.6	295.8	302.9	318.3	1002.7	479.9	329.3
	MLAT	158.1	125.5	110.4	98.2	123.1	346.8	329.7	353.4	309.3	334.8	229.0
	LSQ	299.0	268.9	146.7	487.5	300.5	495.6	440.5	568.8	713.9	554.7	427.6
	MLP	54.1	46.1	34.7	42.6	44.4	95.7	120.3	120.6	125.0	115.4	79.9
	GCN	51.6	44.2	36.1	49.3	45.3	91.5	115.1	117.7	124.3	112.2	78.8
	PNA	50.8	41.3	30.6	38.8	40.4	91.1	115.0	113.9	119.7	109.9	75.2
	GAT	49.7	41.1	30.1	39.2	40.0	89.6	113.7	114.3	117.6	108.8	74.4
	CAGE	42.8	36.5	27.9	35.7	35.7	77.2	101.4	104.1	107.3	97.5	66.6

5.1 Static Evaluation for Jamming Localization

To analyze the impact of node arrangements and sampling coverage on localization accuracy, we evaluate performance in a static setting where devices remain fixed at predefined locations. Each instance consists of nodes randomly placed within the geographic area $\mathcal{A} = \{(x, y) \in \mathbb{R}^2 \mid 0 \leq x, y \leq 1500\}$, following circular, triangular, rectangular, or uniformly random layouts. These configurations define the sampling region $\mathcal{R} \subseteq \mathcal{A}$, where noise floor measurements are collected. The jammer’s position \mathbf{x}_j is also randomly assigned within \mathcal{A} , independently of node placement, resulting in two distinct localization scenarios: when $\mathbf{x}_j \in \mathcal{R}$, proximity to source yields more precise sampling of interference, whereas when $\mathbf{x}_j \in \mathcal{A} \setminus \mathcal{R}$, localization relies on extrapolation from peripheral observations.

Table 1 presents the jammer localization performance across various methods in the static experiment. The classical localization methods exhibit significantly higher errors across all sampling scenarios. Among them, WCL performs best with an overall RMSE of 143.1m, while LSQ yields the worst performance. The suboptimal performance of path-loss-based approaches (PL, MLE, MLAT, LSQ) is likely attributed to their dependency on estimating the path loss exponent (γ) and jammer transmit power (P_t^{jam}) in order to estimate the jammer position [12]. The GNN-based approaches consistently outperform these classical methods. CAGE delivers the highest overall performance, achieving an RMSE of 66.6m,

Table 2: Jammer localization results for dynamic trajectories, reporting MAE and RMSE over three trials. Results are categorized by distance intervals based on the minimum distance d (m) between the jammer and the nearest sampled measurement. The final column reports the overall mean across the entire trajectory, computed considering each s_i^t without skipping intermediate measurements.

	Method	Distance to the Jammer					Mean
		$d > 500$	$d \in [500, 200]$	$d \in [200, 100]$	$d \in [100, 50]$	$d \in [50, 0]$	
MAE	WCL	316.8	220.6	95.2	34.6	7.7	28.2
	PL	323.8	275.3	153.5	74.0	28.9	56.3
	MLE	245.1	130.0	54.2	36.5	1381.8	1006.7
	MLAT	237.8	192.5	122.2	85.8	57.7	73.1
	MLP	140.5 \pm 9.7	83.7 \pm 4.9	35.5 \pm 1.5	21.8 \pm 0.9	14.8 \pm 0.8	20.7 \pm 0.4
	GCN	123.0 \pm 3.8	65.4 \pm 1.0	25.2 \pm 0.1	14.3 \pm 0.2	8.1 \pm 0.2	13.1 \pm 0.1
	PNA	162.1 \pm 5.2	95.1 \pm 2.6	40.9 \pm 2.2	26.3 \pm 1.1	19.5 \pm 1.0	25.7 \pm 1.0
	GAT	88.7 \pm 10.6	49.3 \pm 1.4	23.1 \pm 0.7	13.3 \pm 0.4	7.3 \pm 0.4	11.4 \pm 0.5
	CAGE	73.1\pm0.7	36.7\pm0.9	17.1\pm0.6	9.9\pm0.1	4.2\pm0.1	7.6\pm0.1
RMSE	WCL	372.4	253.1	111.8	45.4	11.6	66.6
	PL	379.8	312.6	190.0	104.2	41.4	100.5
	MLE	510.5	463.9	148.4	92.9	6486.9	5493.5
	MLAT	275.2	234.3	183.9	147.0	99.1	124.7
	MLP	182.1 \pm 9.7	114.8 \pm 7.8	49.1 \pm 3.2	28.3 \pm 1.2	19.0 \pm 1.0	35.0 \pm 0.7
	GCN	161.5 \pm 4.3	91.1 \pm 1.2	34.2 \pm 0.1	19.1 \pm 0.4	10.8 \pm 0.2	25.6 \pm 0.3
	PNA	214.1 \pm 7.3	129.5 \pm 5.2	56.9 \pm 2.4	34.9 \pm 1.7	24.9 \pm 1.1	41.5 \pm 1.2
	GAT	131.0 \pm 13.6	70.0 \pm 0.2	33.2 \pm 1.5	17.8 \pm 0.6	9.6 \pm 0.5	21.3 \pm 0.6
	CAGE	104.0\pm5.9	53.4\pm0.2	23.5\pm0.7	14.0\pm0.4	5.7\pm0.2	15.7\pm0.1

followed by GAT with an RMSE of 74.4m, improving localization accuracy as compared to WCL by 114.9%.

A significant performance gap occurs depending on whether the jammer is located inside or outside the sampled region \mathcal{R} . Localization outside \mathcal{R} is inherently more challenging due to extrapolation beyond measured signals. Classical methods like WCL perform well within densely and radially symmetric sampled regions [25], resulting in an RMSE of 53.3m (inside). However, their performance sharply declines when extrapolating, with RMSE increasing to 232.8m (outside). In contrast, GAT demonstrates better robustness, with RMSE rising moderately from 40.0m (inside) to 108.8m (outside). CAGE achieves the lowest errors overall, with RMSE of 35.7m (inside) and 97.5m (outside). Notably, the circular topology significantly enhances performance when the jammer is outside \mathcal{R} by maximizing angular diversity and preserving directional information. These findings highlight the critical role of spatial coverage and the superior robustness of GNN-based methods for long-range jammer localization.

5.2 Dynamic Evaluation for Jamming Localization

We evaluate localization performance in a dynamic 3D environment where a mobile device navigates through space while tracking a jamming source. The trajectory follows an encirclement pattern, where the device gradually converges toward the jammer while collecting measurements from varying distances and

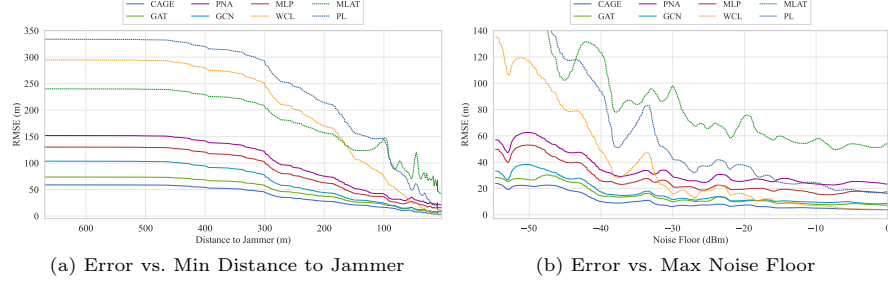


Fig. 2: Localization performance as a function of (a) minimum distance to the jammer and (b) maximum noise floor.

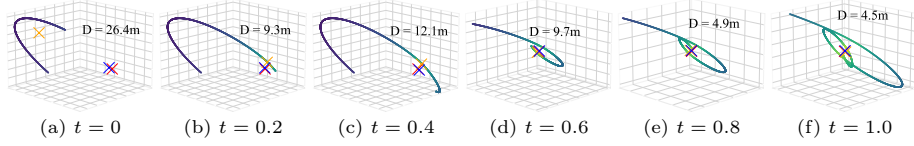


Fig. 3: Localization accuracy along a single trajectory for CAGE. The red cross-mark represents the jammer position, the orange mark represents the WCL reference prediction, and the blue mark represents the model prediction.

angles. This experiment enables the analysis of localization performance under varying observational constraints, evaluating how well methods estimate the jammer’s position with limited initial data and how accuracy evolves as additional spatially diverse measurements are incorporated. During training, we employ random cropping of trajectory segments to expose the model to varied subsequences of the jamming encounter, enhancing robustness to partial observations and improving generalization across different trajectory lengths.

Table 2 presents the jammer localization performance across various methods in the dynamic experiment. The results are categorized by distance intervals, where each column represents a different proximity range between the jammer and the nearest sampled measurement. The final column reports the overall mean across trajectories. Notably, WCL achieves an RMSE of 11.6m in the closest range ($d \in [50, 0]$). However, at larger distances ($d > 500$), WCL degrades significantly with an RMSE of 372.4m. CAGE leverages confidence-weighted estimation to adaptively integrate WCL’s structured prior with the GNN-based predictions, resulting in the most consistent and robust performance. With an RMSE of 5.7m in $d \in [50, 0]$, CAGE significantly outperforms both WCL and GAT. Interestingly, while CAGE integrates WCL as a prior, its benefits extend beyond dense, symmetric scenarios. The performance gap is particularly evident in sparse sampling conditions, where CAGE maintains significantly lower error than WCL and GAT, highlighting its ability to generalize beyond the expected advantages of structured priors.

Table 3: Ablation study on CAGE components.

Loss		Configurations						$\hat{\mathbf{x}}_{\text{final}}$	$\hat{\mathbf{x}}_{\text{GNN}}$
\mathcal{L}_{GNN}	$\mathcal{L}_{\text{Adapt}}$	SN	SN Edges	Con.	Con. In	Reg. In	Con. Out		
✓	✗	✗	—	—	—	●	—	—	21.3±0.6
✗	✓	✓	Undirected	Linear	○	●	Single	22.2±0.2	253.8±40.1
✗	✓	✓	Undirected	Linear	●	●	Single	21.3±0.7	247.4±30.8
✗	✓	✓	No edges	Linear	●	●	Single	20.6±0.1	155.8±32.2
✗	✓	✓	No edges	Linear	○	●	Single	19.7±0.3	119.1±9.2
✗	✓	✓	Directed	Linear	○	●	Single	19.4±0.3	102.9±6.9
✗	✓	✓	Directed	MLP	○	●	Single	18.2±1.1	117.1±4.7
✗	✓	✓	Directed	MLP	○	●	Multiple	17.7±0.4	153.0±17.1
✓	✓	✓	Directed	MLP	○	●	Single	16.6±0.8	16.8±0.8
✓	✓	✓	Directed	MLP	○	●	Multiple	15.7±0.1	16.2±0.0

Figure 2 shows localization performance trends over varying distances to the jammer and noise floor conditions. In Figure 2(a), WCL performs well at short distances, surpassing GAT only very close to the jammer (~ 20 m). GAT exhibits greater robustness over most of the trajectory, while CAGE consistently outperforms both methods. Figure 3 visually compares localization predictions along a trajectory, demonstrating progressive refinement after initial attack detection.

5.3 Ablation Study on CAGE Components

Table 3 presents the ablation study on CAGE components. The columns \mathcal{L}_{GNN} and $\mathcal{L}_{\text{Adapt}}$ indicate the use of graph-based and adaptive losses, respectively. “SN” and “SN Edges” denote the presence of a supernode and the edge type. “Con.” specifies the confidence layer type (linear or 3-layer MLP with ReLU and final sigmoid), while “Con. In” and “Reg. In” indicate the input sources for the confidence layer and regressor. “Con. Out” specifies whether a single or multiple confidence outputs are used. Finally, $\hat{\mathbf{x}}_{\text{final}}$ and $\hat{\mathbf{x}}_{\text{GNN}}$ represent the final estimated position and direct GNN prediction, respectively. The symbols ●, ○, and ○ denote pooled graph representations with a supernode, without a supernode, and exclusively based on the supernode.

Results show that replacing bidirectional edges with directed edges improves accuracy, using an MLP instead of a linear layer reduces RMSE, and multiple confidence outputs outperform a single output. Training with $\mathcal{L}_{\text{CAGE}}$ enables the GNN regressor to function properly, achieving an RMSE of 16.2 compared to 153.0m without it, with adaptive estimation reaching 15.7.

6 Conclusion

This study presents CAGE, a graph-based jammer localization framework that integrates attention-based GNNs with confidence-weighted adaptive estimation. By leveraging spatial priors and learned features, CAGE balances weighted centroid localization with graph-based learning for robust performance across diverse conditions. Evaluations and ablation studies show it outperforms classical

and learning-based methods, especially in generalization beyond observed data and handling noisy and obscure signals.

References

1. Aldosari, W., Zohdy, M., Olawoyin, R.: Jammer localization through smart estimation of jammer's transmission power. In: 2019 IEEE National Aerospace and Electronics Conference (NAECON). pp. 430–436 (2019)
2. Chen, D., O'Bray, L., Borgwardt, K.: Structure-aware transformer for graph representation learning. In: International conference on machine learning. pp. 3469–3489. PMLR (2022)
3. Corso, G., Cavalleri, L., Beaini, D., Liò, P., Veličković, P.: Principal neighbourhood aggregation for graph nets. In: Advances in Neural Information Processing Systems (2020)
4. Ding, K., Xu, Z., Tong, H., Liu, H.: Data augmentation for deep graph learning: A survey. ACM SIGKDD Explorations Newsletter **24**(2), 61–77 (2022)
5. Do, T.H., Nguyen, D.M., Bekoulis, G., Munteanu, A., Deligiannis, N.: Graph convolutional neural networks with node transition probability-based message passing and dropout regularization. Expert Systems with Applications **174**, 114711 (2021)
6. Etiabi, Y., Eldeeb, E., Shehab, M., Njima, W., Alves, H., Alouini, M.S., Amhoud, E.M.: Metagraphloc: A graph-based meta-learning scheme for indoor localization via sensor fusion. arXiv preprint arXiv:2411.17781 (2024)
7. Kipf, T.N., Welling, M.: Semi-supervised classification with graph convolutional networks. In: International Conference on Learning Representations (2017)
8. Lezama, F., Larroca, F., Capdehourat, G.: On the application of graph neural networks for indoor positioning systems. In: Machine Learning for Indoor Localization and Navigation, pp. 239–256. Springer (2023)
9. Li, Q., Han, Z., Wu, X.M.: Deeper insights into graph convolutional networks for semi-supervised learning. In: Proceedings of the AAAI conference on artificial intelligence. vol. 32 (2018)
10. Liu, H., X, W., Chen, Y., Liu, Z.: Localizing jammers in wireless networks. In: 2009 IEEE International Conference on Pervasive Computing and Communications. pp. 1–6 (2009)
11. Merchant, A., Batzner, S., Schoenholz, S.S., Aykol, M., Cheon, G., Cubuk, E.D.: Scaling deep learning for materials discovery. Nature **624**(7990), 80–85 (2023)
12. Nardin, A., Imbiriba, T., Closas, P.: Jamming source localization using augmented physics-based model. In: ICASSP 2023 - 2023 IEEE International Conference on Acoustics, Speech and Signal Processing (ICASSP). pp. 1–5 (2023)
13. Niu, Z., Li, H., Zhou, X., Huang, J.: Overview of jammer localization in wireless sensor networks. In: 2020 IEEE 9th Joint International Information Technology and Artificial Intelligence Conference (ITAIC). vol. 9, pp. 9–13 (2020)
14. Niu, Z., Li, H., Zhou, X., Huang, J.: Overview of jammer localization in wireless sensor networks. In: 2020 IEEE 9th Joint International Information Technology and Artificial Intelligence Conference (ITAIC). vol. 9, pp. 9–13 (2020)
15. Pelechrinis, K., Koutsopoulos, I., Broustis, I., Krishnamurthy, S.V.: Lightweight jammer localization in wireless networks: System design and implementation. In: GLOBECOM 2009 - 2009 IEEE Global Telecommunications Conference. pp. 1–6 (2009)

16. Pirayesh, H., Zeng, H.: Jamming attacks and anti-jamming strategies in wireless networks: A comprehensive survey. *IEEE Communications Surveys & Tutorials* **24**(2), 767–809 (2022)
17. Rappaport, T.S.: *Wireless communications: principles and practice*. Cambridge University Press (1996)
18. Sato, R., Yamada, M., Kashima, H.: Random features strengthen graph neural networks. In: *Proceedings of the 2021 SIAM international conference on data mining (SDM)*. pp. 333–341. SIAM (2021)
19. Sayakkara, A.P., Le-Khac, N.A.: Electromagnetic side-channel analysis for IoT forensics: Challenges, framework, and datasets. *IEEE Access* **9**, 113585–113598 (2021)
20. Srivastava, N., Hinton, G., Krizhevsky, A., Sutskever, I., Salakhutdinov, R.: Dropout: a simple way to prevent neural networks from overfitting. *J. Mach. Learn. Res.* **15**(1), 1929–1958 (Jan 2014)
21. Tedeschi, P., Oligeri, G., Pietro, R.: Localization of a power-modulated jammer. *Sensors* **22** (01 2022)
22. Turkoglu, M.O., Brachmann, E., Schindler, K., Brostow, G.J., Monszpart, A.: Visual camera re-localization using graph neural networks and relative pose supervision. In: *2021 International Conference on 3D Vision (3DV)*. pp. 145–155 (2021)
23. Veličković, P.: Everything is connected: Graph neural networks. *Current Opinion in Structural Biology* **79**, 102538 (2023)
24. Veličković, P., Cucurull, G., Casanova, A., Romero, A., Liò, P., Bengio, Y.: Graph attention networks. In: *International Conference on Learning Representations* (2018)
25. Wang, J., Urriza, P., Han, Y., Cabric, D.: Weighted centroid localization algorithm: Theoretical analysis and distributed implementation. *IEEE Transactions on wireless communications* **10**(10), 3403–3413 (2011)
26. Wang, M., Zheng, D., Ye, Z., Gan, Q., Li, M., Song, X., Zhou, J., Ma, C., Yu, L., Gai, Y., Xiao, T., He, T., Karypis, G., Li, J., Zhang, Z.: Deep graph library: A graph-centric, highly-performant package for graph neural networks. *arXiv preprint arXiv:1909.01315* (2019)
27. Wang, Y., Wang, W., Liang, Y., Cai, Y., Hooi, B.: Graphcrop: Subgraph cropping for graph classification. *arXiv preprint arXiv:2009.10564* (2020)
28. Wei, X., Wang, Q., Wang, T., Fan, J.: Jammer localization in multi-hop wireless network: A comprehensive survey. *IEEE Communications Surveys & Tutorials* **19**(2), 765–799 (2017)
29. Yan, W., Wang, J., Yin, F., Tian, Y., Zoubir, A.M.: Attentional graph neural networks for robust massive network localization. *arXiv preprint arXiv:2311.16856* (2023)
30. Yang, J., Lee, H., Moessner, K.: Multilateration localization based on singular value decomposition for 3d indoor positioning. In: *2016 International Conference on Indoor Positioning and Indoor Navigation (IPIN)*. pp. 1–8 (2016)
31. Yang, Y., Ren, Z., Li, H., Zhou, C., Wang, X., Hua, G.: Learning dynamics via graph neural networks for human pose estimation and tracking. In: *Proceedings of the IEEE/CVF conference on computer vision and pattern recognition*. pp. 8074–8084 (2021)
32. Zhang, M., Li, P.: Nested graph neural networks. *Advances in Neural Information Processing Systems* **34**, 15734–15747 (2021)

A Ablation Studies

We conduct a series of ablation studies to evaluate the impact of different design choices and components on localization performance.

Table 4: Ablations on augmentations, global pooling, and neighborhood size.

(a) Varying number of k nearest neighbors.					(b) Global pooling strategies.				
k	3	5	7	11	Pooling	Sum	Mean	Max	Att
RMSE	54.7 \pm 0.1	57.3 \pm 0.0	60.2 \pm 0.2	64.9 \pm 0.2	RMSE	72.2 \pm 0.3	84.1 \pm 0.2	52.9 \pm 0.1	61.7 \pm 0.3

(c) Graph- and Feature-level augmentations.					
Aug	None	Rotation	Crop	Drop Node	Feat. Noise
RMSE	54.7 \pm 0.1	58.9 \pm 0.1	54.5 \pm 0.1	52.9 \pm 0.1	54.6 \pm 0.1

Table 5: Node feature ablation study.

(a) Static.		(b) Dynamic.	
Node Feature	RMSE (m)	Node Feature	RMSE (m)
Baseline	67.4 \pm 0.1	Baseline	27.4 \pm 0.3
+ $\mathbf{x}_i^{\text{cart}}$	66.0 \pm 0.1 \downarrow 2.1%	+ Moving avg. signal	27.5 \pm 0.3 \uparrow 0.4%
+ d_i^{wcent}	66.0 \pm 0.1 - 0.0 %	+ Path distance	32.7 \pm 0.4 \uparrow 19.3%
+ $\mathbf{x}_i^{\text{wcent}}$	63.6 \pm 0.2 \downarrow 3.6%	+ \mathbf{d}_i	26.2 \pm 0.2 \downarrow 4.4%
+ Azimuth to centroid	66.1 \pm 0.2 \uparrow 0.2%	+ $\Delta\eta_i^{\text{temp}}$	25.6 \pm 0.3 \downarrow 6.6%
+ d_i^{wcent}	63.3 \pm 0.2 \downarrow 0.5%		
+ Azimuth to WC	65.5 \pm 0.5 \uparrow 3.5%		
+ median($\eta_{\mathcal{N}_k(i)}$)	61.3 \pm 0.2 \downarrow 3.2%		
+ max($\eta_{\mathcal{N}_k(i)}$)	59.4 \pm 0.2 \downarrow 3.2%		
+ $\Delta\eta_i$	57.3 \pm 0.0 \downarrow 3.5%		
+ Random feature	57.5 \pm 0.1 \uparrow 0.3%		

A.1 Node Features, Graph Construction, and Augmentations

Table 5 evaluates the impact of various node features in static and dynamic settings using the GCN model on a validation set. Incorporating Cartesian coordinates and weighted centroid distances improves RMSE, while azimuth-based features do not provide benefits. Local noise statistics, particularly mean noise deviation, significantly enhance accuracy. Furthermore, we incorporate unique IDs [18], with which we observe a degradation in performance, possibly due to a loss in the generalization ability of the model [32]. In dynamic scenarios, direction vectors and temporal noise variations further reduce RMSE, highlighting the importance of motion-aware attributes. Table 4 analyzes key graph construction and pooling elements. We find that a lower neighborhood size ($k = 3$) yields best results, with increasing k leading to oversmoothing [9]. Among global pooling

strategies, max pooling achieves the best RMSE. For augmentations, DropNode [5] with a 0.2 drop rate leads to the best improvement. For more information on the augmentation experiments, refer to Appendix A.

A.2 Data Augmentations

In this section, we present additional experiments related to data augmentations, including feature corruption, rotation augmentation, DropNode [5], and random cropping. Feature corruption [4] applies Gaussian noise to a randomly selected subset of node features. Up to half of the total features in each vector are chosen, and a mask determines which node values receive noise with probability p . Rotation augmentation rotates the graph by a random angle between 0 and 360 degrees to encourage orientation invariance. DropNode removes nodes with a drop rate of p . The scaling factor is deliberately excluded to maintain the integrity of physical relationships. Random cropping selects a portion of the graph by identifying the three nodes with the highest noise levels and extending to a randomly chosen endpoint. Although we recognize the preexisting GraphCrop augmentation[27], this method is not relevant for our application which is characterized by uniform node degree and localized areas of importance in the graph. Table 4 presents the results of these experiments, showing that the best performance is achieved with DropNode at $p = 0.2$. Consequently, we adopt this setting exclusively during training, as discussed in Section 5.

Table 6: Performance comparison of different augmentation techniques.

Augmentation	p	RMSE
Feature Noise	1.0	55.0 \pm 0.1
Feature Noise	0.5	54.6 \pm 0.1
Feature Noise	0.1	54.7 \pm 0.1
DropNode	0.5	54.7 \pm 0.2
DropNode	0.2	52.9\pm0.1
DropNode	0.1	53.3 \pm 0.1

We also evaluate combined augmentation strategies where Crop+DN refers to cropping followed by DropNode, DN+Feat Noise represents DropNode followed by feature corruption, and Crop+Feat Noise denotes cropping followed by feature corruption. Table 7 illustrates that combining these augmentations does not significantly improve performance. The best result is achieved with DN + Feat Noise, reinforcing our decision to use DropNode with $p = 0.2$ exclusively.

Table 7: Performance of combined augmentation strategies.

Aug	Crop+DN	DN+Feat Noise	Crop+Feat Noise
RMSE	55.5 \pm 0.1	53.0\pm0.1	55.3 \pm 0.2

B Analysis of Confidence Weighting in CAGE

We analyze how the $\mathcal{L}_{\text{CAGE}}$ loss shapes confidence weight assignment in CAGE. To do so, we compare two training setups: one using only $\mathcal{L}_{\text{Adapt}}$ and another incorporating the full $\mathcal{L}_{\text{CAGE}}$ loss. Confidence weights are plotted against the jammer’s distance to analyze how the choice of loss function affects the model’s reliance on the WCL prior versus GNN-based predictions. This experiment is conducted using dynamic experiment data, described in Section 5.2, where the trajectory follows an encirclement pattern, gradually converging toward the jammer while collecting measurements from varying distances and angles.

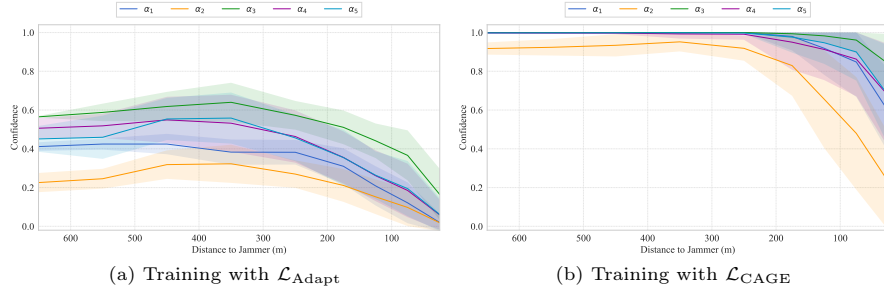


Fig. 4: Effect of training loss on confidence weighting in CAGE. (a) Training with $\mathcal{L}_{\text{Adapt}}$ causes over-reliance on WCL due to low GNN confidence. (b) Training with $\mathcal{L}_{\text{CAGE}}$ increases initial GNN confidence and sharpens the transition near the jammer.

When training solely with $\mathcal{L}_{\text{Adapt}}$ (Figure 4a), the confidence weights remain relatively low even at large distances, indicating that the model strongly relies on WCL across all regions, even where GNN-based predictions should be more informative. Since the final prediction is computed as a weighted combination in Equation (12), higher confidence weights (α) indicate greater reliance on the GNN-based prediction, while lower weights shift reliance toward WCL. Because $\mathcal{L}_{\text{Adapt}}$ only minimizes blended prediction error, it fails to enforce a direct learning signal for the GNN, causing it to act as a correction to WCL rather than as an independent predictor.

In contrast, when $\mathcal{L}_{\text{CAGE}}$ is used (Figure 4b), the confidence weights start much higher ($\alpha \approx 1$), showing that the model correctly prioritizes GNN-based predictions in sparse sampling scenarios. As the distance to the jammer de-

creases, confidence in WCL increases, suggesting that the model has learned to recognize when WCL becomes reliable due to dense sampling and radial symmetry at close distances, which is a characteristic of the data used for this experiment. This improvement stems from enforcing independent learning on \mathcal{L}_{GNN} when predicting the jammer’s position. Ultimately, incorporating $\mathcal{L}_{\text{CAGE}}$ results in a more structured confidence-weighting mechanism, leading to improved robustness and localization accuracy.

Figure 4b also reveals that among all confidence weights, α_2 , which corresponds to $\sin(\theta)$ in the final estimation, remains slightly lower than the others, even at large distances. This indicates that the model retains a small but consistent reliance on the azimuth component of the WCL estimate, even when predominantly using the GNN-based prediction. The fact that α_2 is consistently below the other confidence values suggests that while the model learns to prioritize the GNN overall, it still leverages the WCL azimuth as a stable directional reference. Fine-tuning λ in Equation (14) allows for adjusting the model’s reliance on different components, with $\lambda = 0$ used in this work.

C Further Results and Analysis

Figure 5 illustrates the impact of varying parameters, such as jammer power, network density, and shadowing effects, on localization performance for CAGE, GAT, and WCL on the static experiment data. Across all conditions, CAGE consistently achieves the lowest RMSE, highlighting its robustness. Stronger shadowing (σ) degrades performance across all methods due to increased signal uncertainty [21]. An inverse relationship between jammer power and localization accuracy emerges, likely because lower power forces nodes closer to the jammer, improving localization (see Table 1). As shown in Appendix F, Table 10, the 2D graphs predominantly consists of instances with a small number of nodes. This imbalance limits the model’s exposure to such graphs, leading to degraded performance on larger graphs. The lack of sufficient representation may contribute to feature explosions, a phenomenon consistent with prior findings [3].

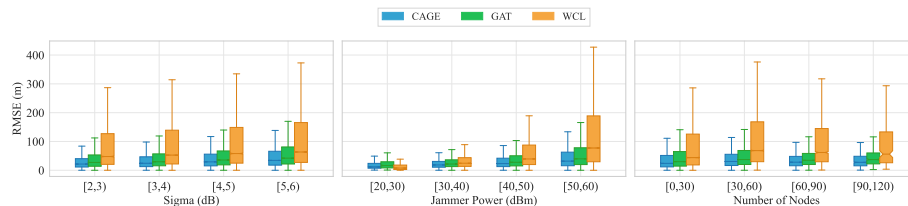


Fig. 5: RMSE analysis of the CAGE, GAT and WCL models across all topologies under the LDPL environment with varying shadowing effects, jammer transmit powers, and number of nodes per graph.

D Downsampling

In real-world scenarios involving Software Defined Radio (SDR) devices, high-frequency signal sampling results in dense, high-resolution data [19], often reaching thousands of nodes per graph, as observed in our dynamic experiments, which contain approximately 6000 nodes per instance (See Appendix F Table 10). We explore downsampling techniques that preserve critical signal characteristics to mitigate computational overhead while retaining the most relevant information.

We evaluate two approaches: (1) *window averaging*, and (2) *spatial binning with noise filtering*. The window averaging method segments the data into equal-sized windows based on the maximum number of nodes. Within each window, node positions and noise values are averaged to produce a single representative node, smoothing short-term fluctuations and ensuring a uniform representation. The second approach applies spatial binning, grouping nodes within fixed 1m^2 grid cells to prevent oversampling in localized regions and ensure spatial coverage. After binning, noise filtering retains only nodes with the highest noise values, under the assumption that weak power observations contribute less to localization accuracy [12]. This step enhances the informativeness of the downsampled data by prioritizing regions with higher noise levels, which are more indicative of environmental and signal propagation conditions.

The ablation results in Table 8 indicate that spatial binning with noise filtering outperforms window averaging, particularly in the later segments of the trajectory, where maintaining high-information nodes is crucial. Based on these findings, we adopt the downsampling configuration with 1000 nodes using spatial binning and noise filtering for our experiments.

Table 8: Ablation study of downsampling techniques on high-resolution dynamic path data under the LDPL model. The table compares the performance of window averaging and spatial binning with noise filtering across different numbers of retained nodes ($|V|$).

$ V $	Window averaging				Spatial binning with noise filtering			
	$t_{0.0-0.2}$	$t_{0.4-0.6}$	$t_{0.8-1.0}$	Mean	$t_{0.0-0.2}$	$t_{0.4-0.6}$	$t_{0.8-1.0}$	Mean
200	74.5	22.1	13.2	38.7	78.4	21.6	10.5	40.5
600	63.2	21.8	14.7	34.3	63.5	16.3	9.8	31.7
800	57.1	23.9	15.7	32.2	59.3	15.3	10.4	29.7
1000	54.6	23.4	16.5	31.4	54.5	13.7	9.8	27.4

E Training Details and Hyperparameter Tuning

Each model is trained for 300 epochs using the AdamW optimizer, with weights initialized via Xavier initialization [26]. The learning rate is linearly warmed up over the first 20% of the total epochs and then follows a cosine annealing schedule. Dropout is set to 0.5 [20] and is applied to graph representations before the final linear layers for all models, except for CAGE, where it is set to 0, as this configuration was found to yield the best results. Weight decay is fixed at 10^{-5} for all models.

We perform hyperparameter tuning using the Tree-structured Parzen Estimator (TPE) sampler and Hyperband pruner for MLP, GCN, and GAT. PNA hyperparameters follow [2], utilizing mean, maximum, and standard deviation as node feature aggregators. The minimum aggregator was excluded as it degraded performance. The hyperparameters for each model are summarized in Table 9, where “LR” denotes learning rate, “WD” refers to weight decay, “BS” represents batch size, “DO” indicates dropout rate, “NH” corresponds to the number of attention heads (for applicable models), “NL” is the number of layers, and “HC/OC” represents the number of hidden and output channels, respectively.

Table 9: Model hyperparameter tuning results, detailing the optimized learning rates (LR), weight decay (WD), batch sizes (BS), dropout rates (DO), number of attention heads (NH), number of layers (NL), and hidden/output channels (HC/OC) for each model.

Model	LR	WD	BS	DO	NH	NL	HC/OC
MLP	0.0004	0.00001	16	0.5	–	8	128 / 64
GCN	0.0005	0.00001	32	0.5	–	2	512 / 256
PNA	0.001	0.00001	128	0.5	–	6	64 / 64
GAT	0.0007	0.00001	8	0.5	4	8	128 / 128

F Signal Propagation and Interference Modeling

This section complements the problem definition by describing how the RSSI, noise floor, and jammer interference are modeled to generate instances for the jammer localization problem. The environment modeling incorporates signal propagation models and the effects of the jammer on the network.

RSSI Modeling The RSSI ($P_{\text{rx},i}$) at a receiving device i from a transmitting device is calculated as:

$$P_{\text{rx},i} = P_t + G_t + G_r - \text{PL}(d_i),$$

where P_t is the transmit power of the transmitting device (in dBm), G_t and G_r are the antenna gains of the transmitting and receiving devices (in dBi), and $\text{PL}(d_i)$ is the path loss (in dB) as defined in Equation (16), determined by the distance d_i between the transmitting and receiving devices and the adopted propagation model.

The path loss $\text{PL}(d_i)$ is modeled for complex NLOS propagation environments using the LDPL model [17]:

$$\text{PL}_{\text{LDPL}}(d) = PL_0 + 10\gamma \log_{10} \left(\frac{d}{d_0} \right) + X_\sigma, \quad (16)$$

where PL_0 is the reference path loss at a reference distance $d_0 = 1$ m, γ is the path loss exponent, and X_σ is the shadowing effect modeled as a Gaussian random variable.

Noise Floor Modeling The noise floor (η_i^t) at device i is the combination of baseline environmental noise and jammer interference, determined using the relevant path loss model. It is expressed in dBm as:

$$\eta_i^t = 10 \cdot \log_{10}(N_{\text{ambient}} + P_{\text{jam},i}),$$

where N_{ambient} is the ambient noise level, and $P_{\text{jam},i}$ is the jammer RSSI at device i , both represented in mW. The ambient noise level is assumed to be -100 dBm. The jammer's RSSI is computed as:

$$P_{\text{jam},i} = P_t^{\text{jam}} + G_t^{\text{jam}} + G_r - \text{PL}(d_{\text{jam},i}),$$

where P_t^{jam} is the jammer's transmit power, G_t^{jam} is its transmitting antenna gain, and $d_{\text{jam},i}$ is the distance from the jammer at location \mathbf{x}_j to device i .

Data Generation We generate 2D (static) and 3D (dynamic) datasets to evaluate localization algorithms. For the static, we create 25,000 samples per topology per jammer placement strategy and 1000 instances for the dynamic dataset, both utilizing LDPL to model signal propagation. Urban and shadowed urban areas are modeled, with path loss exponents ranging from 2.7 to 3.5 and 3.0 to 5.0 [1],

respectively, and moderate to strong shadowing effects between 2 to 6 dB [21], representing physical phenomena which impact the accuracy of signal-based localization techniques [1]. In the static dataset, nodes are placed within the geographic area $\mathcal{A} = \{(x, y) \in \mathbb{R}^2 \mid 0 \leq x, y \leq 1500\}$, with a communication range of 200m. The nodes are arranged in circular, triangular, rectangular, and uniformly random topologies, where the circular and triangular topologies feature a perimeter-bounded node distribution, while a surface-covering node distribution characterizes the rectangular and random topologies. The number of nodes is determined using a beta-distributed scaling factor within a calculated minimum and maximum range, allowing for variability in network densities to simulate different levels of congestion or sparsity. The dataset captures scenarios of both fully jammed or partially jammed networks, ensuring at least one node records a noise floor above -80 dBm, and at least three nodes are jammed to distinguish jamming effects from natural signal fading. For the dynamic dataset, the geographical area of the trajectory is $\mathcal{A} = \{(x, y, z) \in \mathbb{R}^3 \mid 0 \leq x, y \leq 500, 0 \leq z \leq 50\}$, though device motion may extend beyond these bounds during simulation. Further information regarding dataset statistics can be found in 10. For reproducibility, we share the data at <https://www.kaggle.com/datasets/daniaherzalla/network-jamming-simulation-dataset>.

Table 10: Datasets statistics reported for number of nodes per graph (Nodes), noise floor (η), jammer transmit power (P_t^{jam}), shadowing (X_σ), path loss exponent (γ), and distance of graph centroid to jammer (D_{jam}).

Data	Feature	Mean	Min/Max
Static	Nodes	33.6 \pm 19.1	3.0/122.0
	η	-63.9 \pm 13.3	-100.0/72.4
	P_t^{jam}	51.1 \pm 6.3	20.0/59.0
	X_σ	4.2 \pm 1.2	2.0/6.0
	γ	3.1 \pm 0.3	2.7/5.0
	D_{jam}	674.6 \pm 392.6	0.1/2117.4
Dynamic	Nodes	5809.0 \pm 5527.7	1112.0/37144.0
	η	-56.6 \pm 18.6	-80.0/19.9
	P_t^{jam}	39.3 \pm 11.9	20.0/60.0
	X_σ	4.0 \pm 1.1	2.0/6.0
	γ	3.1 \pm 0.2	2.7/3.5
	D_{jam}	295.2 \pm 349.5	3.0/2184.7